

Topological Magneto-optical Kerr Effect without Spin-orbit Coupling in Spin-compensated Antiferromagnet

Camron Farhang,^{1,+} Weihang Lu,^{1,+} Kai Du,² Yunpeng Gao,³ Junjie Yang,³ Sang-Wook Cheong,² and Jing Xia^{1,*}

¹ Department of Physics and Astronomy, University of California, Irvine, Irvine, CA 92697, USA

² Keck Center for Quantum Magnetism and Department of Physics and Astronomy, Rutgers University, Piscataway, NJ 08854, USA.

³ Department of Physics, New Jersey Institute of Technology, Newark, New Jersey 07102, USA

+These authors contributed equally.

*Correspondence: xia.jing@uci.edu

The magneto-optical Kerr effect (MOKE), the differential reflection of oppositely circularly polarized light, has traditionally been associated with relativistic spin-orbit coupling (SOC), which links a particle's spin with its orbital motion. In ferromagnets, large MOKE signals arise from the combination of magnetization and SOC, while in certain coplanar antiferromagnets, SOC-induced Berry curvature enables MOKE despite zero net magnetization. Theoretically, large MOKE can also arise in a broader class of magnetic materials with compensated spins, without relying on SOC - for example, in systems exhibiting real-space scalar spin chirality. The experimental verification has remained elusive. Here, we demonstrate such a SOC- and magnetization-free MOKE in the noncoplanar antiferromagnet $\text{Co}_{1/3}\text{TaS}_2$. Using a Sagnac interferometer microscope, we image domains of scalar spin chirality and their reversal. Our findings establish experimentally a new mechanism for generating large MOKE signals and position chiral spin textures in compensated magnets as a compelling platform for ultrafast, stray-field-immune opto-spintronic applications.

The magneto-optical Faraday ¹ and Kerr ² effects, which reflect the fundamental interactions between circularly polarized light and magnetic materials, have been known for over a century. Among them, the magneto-optical Kerr effect (MOKE) has been extensively utilized for probing magnetic properties ³, visualizing magnetic domains ², manipulating magnetic order ⁴, and enabling a variety of magneto-optical technologies ⁵, even down to the two-dimensional (2D) limit ^{6,7}.

Spin-orbit coupling (SOC) ^{8,9}, a relativistic interaction between a particle's spin and its orbital motion, has been deemed central in generating large MOKE signals. The presence of MOKE in ferromagnets has been attributed to the interplay between SOC and band exchange splitting (BES) in the band structure ¹⁰ induced by either the spontaneous magnetization or an external magnetic field. In non-collinear antiferromagnets with negligible net magnetization ¹¹, large MOKE signals up to 300 μrad have recently been predicted ¹² and observed ¹³, due to a non-zero net Berry curvature in the band structure induced by SOC. This dependence on SOC appears to be a general requirement: although finite MOKE can be observed in systems such as time-reversal symmetry-breaking superconductors ¹⁴⁻¹⁶ and orbital Hall materials ¹⁷ with negligible SOC, the magnitude of the effect in these cases is typically several orders of magnitude smaller, often in the nanoradian range. With the emergence of novel magnetic materials such as altermagnets ^{18,19}, where SOC and net magnetization are both intrinsically weak or absent, it becomes a question of fundamental significance whether large MOKE signals can be achieved without relying on SOC or net magnetization. This is also of practical importance, as MOKE offers a practical readout for spintronic and opto-spintronic devices based on altermagnets and antiferromagnets of compensated spins, with minimal stray fields, field robustness, and fast switching ²⁰⁻²³.

Theoretically, spin-dependent band splitting, and thus MOKE, can also arise from real-space spin textures of compensated spins without referencing relativistic SOC ²⁴⁻²⁶. For instance, non-relativistic exchange-driven band splitting occurs in itinerant electron systems, giving rise to phenomena like altermagnetism ^{18,19}. One of the simplest examples is a noncoplanar antiferromagnet, proposed to exhibit a novel topological light-matter interaction ²⁴, inducing a topological MOKE signal due to finite scalar spin chirality without relying on SOC or BES, i.e. without a net magnetization. In its minimal configuration as illustrated in Fig. 1a, three noncoplanar twisted spins S_i , S_j , and S_k generate a fictitious U(1) gauge field $b_f \propto t_3 \chi_{ijk} \hat{n}$, where $t_3 = t_{ij} t_{jk} t_{ki}$ is the product of successive electron hopping integrals around the triangular loop $i \rightarrow j \rightarrow k \rightarrow i$, $\chi_{ijk} = S_i \cdot (S_j \times S_k)$ is the scalar spin chirality representing real-space “spin-winding”, and \hat{n} is the unit vector normal to the face of the triangle. This fictitious field b_f originates from the orbital motion of electrons: as an electron hops around the triangle, it acquires a geometric Berry phase ²⁷ corresponding to the solid angle subtended by the three spins. This topologically nontrivial Berry phase results in a phase difference $\Delta\phi$ between left- and right-circularly polarized (LCP and RCP) light upon reflection, manifesting as a Kerr angle $\theta_K = \Delta\phi/2$. Notably, this coupling between spin and orbital

degrees of freedom (spin-dependent band splitting) arises from Kondo exchange coupling between conduction electrons and a noncoplanar arrangement of localized magnetic moments, without requiring relativistic SOC ²⁵.

Despite the promising potential of this SOC-free mechanism for MOKE in compensated magnetic systems, experimental verification has remained elusive. Proposed candidate systems such as $\gamma\text{-Fe}_x\text{Mn}_{1-x}$ and $\gamma\text{-Na}_x\text{CoO}_2$ ²⁴ have not exhibited the expected signatures. This absence is partly due to the limited exploration of non-coplanar antiferromagnetic orders and partly because the fictitious magnetic field arising from scalar spin chirality often cancels out due to symmetry, typically requiring external strain to stabilize a net effect ²⁴. Lastly, the choice of the optical wavelength is non-trivial as the theoretically calculated Kerr signal oscillates strongly with the photon energy, crossing zero frequently ²⁴.

Large MOKE without SOC in $\text{Co}_{1/3}\text{TaS}_2$

In this study, we report the first experimental realization of a large spontaneous MOKE signal of $250\ \mu\text{rad}$ at the technologically relevant telecommunication wavelength of $1550\ \text{nm}$ in the triangular lattice compound $\text{Co}_{1/3}\text{TaS}_2$ ^{28–30}, despite its negligible net magnetization of $0.01\ \mu_B/\text{Co}$. This result confirms the viability of the SOC-free mechanism for producing technologically relevant MOKE signals. Using MOKE imaging, we visualize scalar spin chirality domains and their switching behavior under applied magnetic fields.

$\text{Co}_{1/3}\text{TaS}_2$ belongs to a broader family of magnetic element-intercalated van der Waals transition metal dichalcogenides, which exhibit a wide range of magnetic states depending on the intercalants ^{31–36}. Its crystal structure consists of chiral alternating layers of cobalt, which carry localized magnetic moments, and metallic tantalum disulfide, which hosts itinerant electrons. While neutron scattering studies in the 1980s reported ³³ a magnetic modulation vector of $q_m = (1/3, 1/3, 0)$, leading to interpretations involving a “toroidal” magnetic order ²⁸, recent experiments ^{30,29} on $\text{Co}_{1/3}\text{TaS}_2$ and $\text{Co}_{1/3}\text{NbS}_2$ have instead identified $q_m = (1/2, 0, 0)$. The latter corresponds to a non-coplanar “triple-Q” order ^{30,29}, simultaneously breaking time-reversal and inversion symmetry. Consequently they exhibit anomalous Hall effect ^{37,30,29} and Nernst effect ³⁸ arising from an uncompensated fictitious magnetic field, even though their net magnetic moments are vanishingly small. As illustrated in [Fig.1c](#), the magnetic unit cell in this triple-Q state includes eight triangular plaquettes that generate a strong fictitious field oriented along the crystallographic c-axis. Importantly, this magnetic order does not involve any net spin magnetization; rather, the fictitious field couples to the orbital motion of itinerant electrons, producing a small orbital magnetic moment of approximately $0.01\ \mu_B$ per Co^{2+} ion ^{29,30}.

This spin configuration has non-zero scalar spin chirality and is not associated with any spin rotation symmetry, so non-relativistic spin splitting can occur along any direction. In addition, this spin

configuration can have a net magnetization along c -axis when SOC is included, so it may be considered as an “M-type” altermagnet with magnetic point group of $32'$ ³⁹.

Upon warming, this triple-Q order transitions at the Néel temperature T_{N2} into a single-Q stripe order as illustrated in Fig.2b with zero scalar spin chirality, and subsequently into a paramagnetic state above T_{N1} ²⁹. The $\text{Co}_{1/3}\text{TaS}_2$ crystals used in our experiments were synthesized via chemical vapor transport (Methods), as shown in the inset of Fig.1d. Magnetic susceptibility measurements under field-cooled (FC) and zero-field-cooled (ZFC) conditions (Fig.1b) indicate transition temperatures of $T_{N1} \sim 33 \text{ K}$ and $T_{N2} \sim 16 \text{ K}$.

MOKE detection and imaging are performed using a zero-loop Sagnac interferometer microscope^{6,14,40,41} in the polar geometry (Fig.1e) operating at the most popular telecommunication wavelength of 1550 nm (0.80 eV photon energy). This technique offers exceptional sensitivity, routinely achieving $0.01 \mu\text{rad}$ resolution. This is made possible by its exclusive detection of microscopic time-reversal symmetry breaking (TRSB) while strongly rejecting non-TRSB effects, such as optical birefringence, with a suppression level of 10^{-6} (Supplementary Information). This distinction is particularly important in $\text{Co}_{1/3}\text{TaS}_2$, where some of the authors have recently observed a birefringent polarization rotation of $600 \mu\text{rad} \sin(2\alpha)$ due to a nonvolatile nematic order, with α being the incident polarization angle⁴². The selective sensitivity to TRSB is achieved by using a single-mode optical fiber as both the source and detector for counter-propagating, time-reversed light beams⁴³. According to Onsager’s relations⁴⁴, this configuration guarantees zero signal in the absence of TRSB.

We now present the results of our MOKE measurements. Fig.1d shows the spontaneous MOKE signal θ_K obtained during zero-field warm (ZFW) after $B = 0.3 \text{ T}$ field cool (FC), measured at a single point with $2 \mu\text{m}$ optical beam size. Remarkably, we observe a giant θ_K of $250 \mu\text{rad}$, comparable to the $300 \mu\text{rad}$ signal reported in the coplanar non-collinear antiferromagnet Mn_3Sn ¹³, where the large MOKE arises from relativistic SOC-induced Berry curvature¹². It is important to note that both $\text{Co}_{1/3}\text{TaS}_2$ and Mn_3Sn exhibit vanishingly small net magnetic moments, with values of $\sim 0.01 \mu_B/\text{Co}$ ^{29,30} and $\sim 0.005 \mu_B/\text{Mn}$ ⁴⁵, respectively. This experimental result thus firmly establishes that the SOC-free mechanism driven by the scalar spin chirality can produce MOKE signals on par with those generated by SOC-induced Berry curvature. When compared to theoretical predictions, the calculated θ_K in the proposed triple-Q state of $\gamma\text{-Fe}_x\text{Mn}_{1-x}$ is even larger, reaching $\pm 10 \text{ mrad}$ depending on the photon wavelength²⁴. These observations suggest that the SOC-free mechanism holds substantial promise for approaching the largest reported MOKE of $\sim 10 \text{ mrad}$ in ferromagnets CoPt ⁴⁶.

In contrast to the large θ_K in the triple-Q state, no measurable MOKE signal was detected during ZFW through T_{N2} into the single-Q phase, or upon further warming above T_{N1} into the paramagnetic phase

(Fig.1d). This is consistent with theoretical predictions: both the single-Q and paramagnetic phases lack scalar spin chirality and thus are not expected to support a finite MOKE²⁴.

We observed negligible spontaneous θ_K after zero-field cool (ZFC), indicating the formation of oppositely polarized domains smaller than the optical beam size in the absence of a training field.

Fig.2a summarizes the MOKE hysteresis loops across different magnetic phases of $\text{Co}_{1/3}\text{TaS}_2$. At 50 K, in the paramagnetic phase, the Kerr signal θ_K exhibits a small linear response to the applied magnetic field B , consistent with partial alignment of magnetic moments by the external field. At 20 K, in the single-Q phase as illustrated in Fig. 2b, the MOKE signal develops a shallow S-shaped curve but remains zero at zero field, consistent with the absence of scalar spin chirality χ_{ijk} . Upon cooling to 15 K, as the system enters the non-coplanar triple-Q phase, a small hysteresis loop emerges between ± 0.4 T (cyan curve in Fig. 2a), signaling the onset of a finite χ_{ijk} and the associated fictitious field b_f . Notably, across ~ 5 T magnetic field, there is a smooth change in the Kerr signal, corresponding to a metamagnetic transition into a different magnetic configuration^{29,30}, referred to here as the triple-Q' state. Further cooling to 10 K, 5 K, and 2 K leads to increasingly wide and pronounced hysteresis loops, indicating higher coercive fields required to reverse the chirality domains and stronger fictitious fields at zero applied field. The jump in MOKE signal across 5 T field also becomes more abrupt at lower temperatures, signifying a sharper metamagnetic transition between the triple-Q and triple-Q' phases.

The most striking feature of the Kerr hysteresis in the triple-Q phase (Fig.2a) is its field independence: once the sign of χ_{ijk} is established by the external field, the Kerr signal remains nearly constant between 0 T and 4 T fields. A similar plateau is observed in the triple-Q' phase above 6 T. For clarity, the 2 K MOKE hysteresis is replotted in Fig. 2d, revealing a stark contrast to the corresponding 2 K magnetization M_z (Fig. 2c). M_z begins at $\sim 0.01 \mu_B$ per Co at zero field and increases linearly at a rate of $dM_z/dB \sim 0.02 \mu_B/T$, except for a discrete jump of $\sim 0.07 \mu_B$ at 5 T due to the metamagnetic transition. This contrasting field dependence between MOKE and M_z confirms their decoupling: while MOKE arises from the fictitious field b_f generated by scalar spin chirality, the magnetization includes both spin and orbital contributions. Specifically, the zero-field M_z and its linear slope dM_z/dB are due to the orbital moment of itinerant electrons, induced respectively by the fictitious field b_f and the external magnetic field B . These orbital contributions are not directly coupled to the Kerr signal. In contrast, the metamagnetic transition, which involves a spin reconfiguration, produces simultaneous step-like changes in both M_z and θ_K . Importantly the optical reflectivity remained constant to within 0.5% during the entire measurement (Fig. 2g), confirming that the metamagnetic transition represents a change of the spin configuration and has minimum impacts on the electronic structure.

Since the nature of the metamagnetic transition has not been resolved by neutron scattering experiments yet^{29,30}, we adopt a simplified working assumption: the transition reflects a sudden change in the angle θ between spins S_1 and S_4 , as illustrated in the inset of Fig. 2d. Under this assumption, the net spin moment is given by $M_{\text{spin}} = \frac{1}{2}(-1 - 3 \cos(\theta)) \mu_B$, assuming a *g-factor* of -2. And it can be estimated experimentally from magnetization as $M_{\text{spin}} \sim M_z - 0.02 \mu_B \cdot B$, accounting for the orbital contribution. The scalar spin chirality χ_{ijk} is assumed to scale with the bottom triangular plaquette $\chi_{ijk} \propto \chi_{123} \propto -\frac{3}{2}\sqrt{3} \cos(\theta) \sin(\theta)^2$. Within this simplistic model, we estimate $\chi_{ijk} \sim -\frac{2(1+2M_{\text{spin}})(-2+M_{\text{spin}}+M_{\text{spin}}^2)}{3\sqrt{3}}$, as plotted in Fig. 2f. Comparing this estimated χ_{ijk} and the measured θ_K (Fig. 2d), the model qualitatively captures the key features of the magnetic-field dependence of MOKE. The quantitative discrepancy across the transition across 5 T suggests that a more accurate model is required for this metamagnetic transition. This will depend on resolving the spin structure of the triple-Q' phase in future neutron scattering experiments, beyond the scope of the present work. Lastly, we note the DC Hall effect σ_{xy} (Fig. 2e) shows an opposite change across the metamagnetic transition, suggesting a rather complex frequency dependence related to the corresponding change of spin texture across the metamagnetic transition.

Imaging scalar spin chirality domains and chemical inhomogeneity

MOKE microscopy provides a powerful, non-contact method for imaging spin chirality domains and their associated dynamics. One immediate application is the assessment of chemical inhomogeneity. Recent neutron scattering and transport studies⁴⁷ have reported that even slight variations in cobalt composition ($0.30 < x < 0.34$) can lead to significant changes in the physical properties of Co_xTaS_2 . It is therefore critical to determine the extent of chemical inhomogeneity, and its impact on the MOKE signal within a single crystal.

In Fig. 3, we present a combined study of optical reflectivity imaging, MOKE imaging, and single location MOKE hysteresis, all performed at 2 K. The optical reflectivity map (Fig. 3b) is largely uniform with $0.42 < R < 0.44$, which we use as a convenient proxy for cobalt composition as it is difficult to perform energy dispersive x-ray spectroscopy chemical mapping in the same region. MOKE hysteresis loops measured at a few representative locations with varying reflectivity values are shown in Fig. 3a. All locations exhibit nearly identical coercive fields of ~ 0.8 T, with the primary variation being in the zero-field Kerr signal (200, 202, 160, and 80 μrad , respectively). To further examine the magnetic inhomogeneity, we performed MOKE imaging at three key points along the hysteresis loop: at zero field (Fig. 3d), and near the switching fields at -1 T (Fig. 3e) and $+0.8$ T (Fig. 3e). Near the switching fields,

large variations in both positive and negative Kerr signals are observed (Fig. 3c, e), consistent with the coexistence and reversal of spin chirality domains across the sample. Importantly, the spatial patterns seen in Figs. 3c and 3e do not resemble those in the reflectivity map (Fig. 3b), suggesting that the coercive field and domain switching behavior are not strongly correlated with cobalt composition. Instead, they are likely influenced by local strain, defects, or other extrinsic structural factors.

In stark contrast, a clear correlation emerges between the optical reflectivity (Fig. 3b) and the zero-field MOKE image (Fig. 3d), where the chirality has been uniformly trained to a negative value. This observation implies that cobalt composition primarily affects the magnitude of the MOKE signal in the zero-field state, rather than the switching dynamics. To further test this hypothesis, we investigated a rare inhomogeneous region (see Extended Data Fig. 1) where reflectivity varies significantly from 0.40 to 0.45. In this region, the spontaneous MOKE signal ranges from $-40 \mu\text{rad}$ to $-180 \mu\text{rad}$. A plot of MOKE vs. reflectivity in Extended Data Fig. 1 reveals an empirical linear relationship within this limited reflectivity range, supporting the idea that local cobalt concentration modulates the amplitude of the Kerr signal.

Imaging scalar spin chirality domain reversal

Having established that most of the sample is magnetically uniform, we now demonstrate the utility of MOKE microscopy in visualizing scalar spin chirality domain reversal under an external magnetic field. These measurements were conducted in magnetically homogeneous regions at an elevated temperature of 10 K, where domain reversal occurs over a broader field range. The results are shown in Fig. 4 and Extended Data Fig. 2.

A sequence of MOKE images from a uniform region is presented in Figs. 4b-i, with the corresponding local hysteresis loop taken at a single location shown in Fig. 4a. At $B = -9 \text{ T}$ (Fig. 4b), the MOKE signal is uniformly negative ($\theta_K \sim -200 \mu\text{rad}$, shown in blue), except for a few isolated spots that are likely regions of differing Co composition with near-zero Kerr signals (green). At $B = 0$ (Fig. 4c), patches with $\theta_K \sim 0$ begin to emerge. These are interpreted as sub-wavelength domains with mixed positive and negative chiralities, whose contributions average to near zero within the $\sim 2 \mu\text{m}$ optical spot size. As the magnetic field increases (Figs. 4d-f), these green regions grow and are joined by new areas exhibiting positive chirality (orange to red). The positive domains progressively expand through domain wall motion, eventually dominating the lower half (Fig. 4g) and finally the entire imaged region (Fig. 4h-i), culminating in a uniform positive Kerr signal of $\theta_K \sim 200 \mu\text{rad}$.

Notably, even at a low field of 0.1 T (Fig. 4d), isolated positive domains are already present. This indicates that the coercive field for domain reversal is not fundamentally dictated by the intrinsic non-coplanar magnetic phase but is instead governed by extrinsic factors such as local strain, defects, or pinning centers. This insight suggests that by engineering these extrinsic factors, it may be possible to tailor coercive

fields in $\text{Co}_{1/3}\text{TaS}_2$ and related materials, either minimizing them for low-power logic switching applications or maximizing them for robust spin memory devices.

Further evidence of this chirality domain reversal dynamics is provided in [Extended Data Fig. 2](#), which presents MOKE images of another region taken at 1 T intervals across the full field sweep. As in the main data, domain reversal near ± 1 T occurs via domain wall motion, with positive and negative chirality domains coexisting during the transition.

Interestingly, [Extended Data Fig. 2](#) also captures the distinct dynamics of the metamagnetic transition, which occurs gradually between $B = 4$ T and 6 T. Across the 3 T \rightarrow 9 T \rightarrow 3 T cycle, the MOKE signal changes smoothly and uniformly across the field of view, with no evidence of domain wall motion. This behavior resembles a coherent rotation process in ferromagnetic hysteresis, and implies that the critical field for the metamagnetic transition is determined by the intrinsic spin structure transformation. This conclusion is supported by the consistent metamagnetic transition field observed across different samples and temperatures^{30,29}. Finally, [Extended Data Fig. 3](#) shows a zero-field MOKE image taken at 20 K in the single-Q phase. The MOKE signal is uniformly zero across the imaged region, consistent with the expectation that scalar spin chirality, hence MOKE, is absent in the single-Q phase.

Discussion

The observed topological MOKE in $\text{Co}_{1/3}\text{TaS}_2$ represents a fundamentally new form of light-matter interaction arising from the chirality of real-space spin textures composed of compensated spin moments, an effect predicted by theory²⁴ but not previously observed. Unlike conventional MOKE mechanisms that depend on relativistic spin-orbit coupling of individual spins or a net spin moment^{10,12}, this SOC-free mechanism is rooted in the collective topology of the real-space spin texture with compensated spins. It is therefore expected to apply to a much broader class of magnetic materials with “winding” real-space spin configurations. It is noted that although SOC is not required for the topological MOKE discussed here, it can slightly modify its strength, as shown in theoretical studies of topological Hall conductivity in the DC limit⁴⁸.

[Extended Data Fig. 2](#) compares the topological MOKE-over-magnetization ratio (θ_K/M) in $\text{Co}_{1/3}\text{TaS}_2$ with other magnetic systems. In ferromagnets (Ni⁴⁹, Fe⁴⁹, and CoPt⁴⁶), spontaneous θ_K scales with remanent magnetization due to SOC, following a ~ 0.03 rad/ μ_B ratio. In contrast, Noncoplanar antiferromagnet $\text{Co}_{1/3}\text{TaS}_2$ and coplanar antiferromagnet Mn_3Sn ¹³ exhibit much larger θ_K/M ratios due to negligible net magnetization ($0.005 - 0.01 \mu_B$). It is important to note that while MOKE in Mn_3Sn is driven by SOC-induced Berry curvature, MOKE in $\text{Co}_{1/3}\text{TaS}_2$ arises from real-space scalar spin chirality. The skyrmion lattice phase in Gd_2PdSi_2 ⁵⁰ has a topological contribution to MOKE from swirling spins, though limited to a narrow field range and a large net moment of $4 \mu_B$.

Using the noncoplanar spin system in $\text{Co}_{1/3}\text{TaS}_2$ ^{28,30,29} as a model system, we demonstrated this mechanism's efficacy and employed MOKE microscopy to image both chiral domain reversal and the metamagnetic transition. The observed giant spontaneous MOKE at telecommunication wavelengths is readily detectable using standard experimental setups. Moreover, theoretical work predicts that at terahertz frequencies, this system can host a quantum topological Kerr effect with a quantized Kerr rotation of $\pi/2$ ²⁴, surpassing all known magneto-optical materials in magnitude.

These findings have direct implications for advancing antiferromagnet and antiferromagnet-based spintronics and opto-spintronics^{20–23}. Devices based on this SOC-free mechanism would inherently be immune to stray magnetic fields and capable of ultrafast switching, overcoming key limitations of traditional ferromagnetic technologies. MOKE is well suited for ultrafast, local detection of spin-chirality domain switching driven by chiral spin-orbit torques from electric current or circularly polarized light. More broadly, this mechanism relaxes the design constraints imposed by SOC-based magneto-optical materials, offering greater flexibility in engineering materials with tailored magneto-optical responses. We envision that SOC-free magneto-optical materials, especially the van der Waals layers, can be realized through diverse fabrication techniques, including nanofabrication, molecular beam epitaxy, layer stacking, and self-assembly. This opens a wide and largely unexplored landscape for next-generation magneto-optical materials and devices.

Methods:

Crystal Growth:

$\text{Co}_{1/3}\text{TaS}_2$ single crystals were grown by chemical vapor transport method. The powder samples of $\text{Co}_{1/3}\text{TaS}_2$ were synthesized first using the solid-state reaction method. High-purity powders of Cr (99.97%), Ta (99.9%), and S (99.999%) were mixed in stoichiometric ratios. The mixed powders were ground, pelletized, and sealed in quartz tubes. The pellets of powder were then sintered at 750 °C for 48 hours at a heating rate of ~15 °C/h, with intermediate grinding. For the single-crystal growth of $\text{Co}_{1/3}\text{TaS}_2$, the resulting black powder samples were sealed in evacuated quartz tubes together with iodine (I_2) as a transport agent. The tubes were placed in a two-zone furnace for 10 days, where the hot and cold ends were maintained at 1000 °C and 900 °C, respectively. The resulting crystals are hexagonal plate-like.

Magnetization measurements:

The magnetic susceptibility versus temperature (χ -T) curves were measured using a Cryogenic-Limited Cryogen Free Measurement System (CFMS) with a vibrating sample magnetometer (VSM) option. A magnetic field of 0.1 T was applied along the c-axis of the $\text{Co}_{1/3}\text{TaS}_2$ single crystal during the measurements of χ -T curves. The magnetic moment versus magnetic field (M-H) curves were also measured using the VSM option of our CFMS. The crystal was first cooled to base temperature in a zero magnetic field, then the M-H curve was measured by ramping up the magnetic field.

Hall measurements:

The Hall effects of the sample were characterized by a Keithley 2182 Nanovoltmeter and Keithley 6221 Current Source, and the sample temperature and magnetic field were controlled by the CFMS system. During the measurement, an electric current of 1 mA was applied along the ab plane of the crystal, and the magnetic field was applied to the c-axis of the crystal.

Sagnac MOKE measurements are performed using a zero-loop fiber-optic Sagnac interferometer as shown in [Fig. 1c](#). The beam of light is routed by a fiber circulator to a fiber polarizer. After the polarizer the polarization of the beam is at 45° to the axis of a fiber-coupled electro-optic modulator (EOM), which generates 4.6 MHz time-varying phase shifts $\phi_m \sin(\omega t)$, where the amplitude $\phi_m = 0.92$ rad between the two orthogonal polarizations that are then launched into the fast and slow axes of a polarization maintaining (PM) single-mode fiber. Upon exiting the fiber, the two orthogonally polarized linearly polarized beams are converted into right- and left-circularly polarizations by a quarter-wave plate (QWP) and are then focused onto the sample. After reflection from the sample, the same QWP converts the reflected beams back into linear polarizations with exchanged polarization axes. The two beams then pass

through the PM fiber and EOM but with exchanged polarization modes in the fiber and the EOM. At this point, the two beams have gone through the same path but in opposite directions, except for a phase difference of $\Delta\varphi$ from reflection off the magnetic sample and another time-varying phase difference by the modulation of EOM. This nonreciprocal phase shift $\Delta\varphi$ between the two counterpropagating circularly polarized beams upon reflection from the sample is twice the Kerr rotation $\Delta\varphi = 2\theta_K$. The two beams are once again combined at the detector and interfere to produce an optical signal $P(t)$:

$$P(t) = \frac{1}{2} P[1 + \cos(\Delta\varphi + \phi_m \sin(\omega t))]$$

, where P is the returned power if the modulation by the EOM is turned off. For MOKE signals that are slower than the 4.6 MHz modulation frequency used in this experiment, we can treat $\Delta\varphi$ as a slowly time-varying quantity. And $P(t)$ can be further expanded into Fourier series with the first few orders listed below:

$$\begin{aligned} P(t)/P &= \frac{1}{2} [1 + J_0(2\phi_m)] \\ &\quad + (\sin(\Delta\varphi) J_1(2\phi_m)) \sin(\omega t) \\ &\quad + (\cos(\Delta\varphi) J_2(2\phi_m)) \cos(2\omega t) \\ &\quad + 2 J_3(2\phi_m) \sin(3\omega t) \\ &\quad + \dots \end{aligned}$$

, where $J_1(2\phi_m)$ and $J_2(2\phi_m)$ are Bessel J-functions. Lock-in detection was used to measure the first three Fourier components: the average (DC) power (P_0), the first harmonics (P_1), and the second harmonics (P_2). And the Kerr rotation can then be extracted using the following formula:

$$\theta_K = \frac{1}{2} \Delta\varphi = \frac{1}{2} \tan^{-1} \left[\frac{J_2(2\phi_m)P_1}{J_1(2\phi_m)P_2} \right]$$

Acknowledgements

This project was supported by NSF award DMR-2419425 and the Gordon and Betty Moore Foundation EPiQS Initiative, Grant # GBMF10276. The work at Rutgers University was supported by the DOE under Grant No. DOE: DE-FG02-07ER46382. J.Y. acknowledges support by DOE under Grant No. DOE: DE-SC0021188.

Author Contributions

J.X. conceived and supervised the project. C.F., W.L., and J.X. carried out the optical measurements. K.D., Y.G., J.J., and S.W.C. grew the crystals and carried out transport and magnetization measurements. J.X. drafted the paper with the input from all authors. All authors contributed to the discussion of the manuscript.

Competing interests

The authors declare no competing interest.

References:

1. Experimental researches in electricity.-Nineteenth series. *Phil. Trans. R. Soc.* **136**, 1–20 (1846).
2. Kerr, J. On rotation of the plane of polarization by reflection from the pole of a magnet. *The London, Edinburgh, and Dublin Philosophical Magazine and Journal of Science* **3**, 321–343 (1877).
3. Qiu, Z. Surface magneto-optic Kerr effect (SMOKE). *Journal of Magnetism and Magnetic Materials* **200**, 664–678 (1999).
4. Kirilyuk, A., Kimel, A. V. & Rasing, T. Ultrafast optical manipulation of magnetic order. *Rev. Mod. Phys.* **82**, 2731–2784 (2010).
5. Mansuripur, M. *The Physical Principles of Magneto-Optical Recording*. (Cambridge University Press, 1995). doi:10.1017/CBO9780511622472.
6. Gong, C. *et al.* Discovery of intrinsic ferromagnetism in two-dimensional van der Waals crystals. *Nature* **546**, 265–269 (2017).
7. Huang, B. *et al.* Layer-dependent ferromagnetism in a van der Waals crystal down to the monolayer limit. *Nature* **546**, 270–273 (2017).
8. Thomas, L. H. The Motion of the Spinning Electron. *Nature* **117**, 514–514 (1926).
9. Fröhlich, J. & Studer, U. M. Gauge invariance and current algebra in nonrelativistic many-body theory. *Rev. Mod. Phys.* **65**, 733–802 (1993).
10. Argyres, P. N. Theory of the Faraday and Kerr Effects in Ferromagnetics. *Phys. Rev.* **97**, 334–345 (1955).
11. Chen, H., Niu, Q. & MacDonald, A. H. Anomalous Hall Effect Arising from Noncollinear Antiferromagnetism. *Phys. Rev. Lett.* **112**, 017205 (2014).
12. Feng, W., Guo, G.-Y., Zhou, J., Yao, Y. & Niu, Q. Large magneto-optical Kerr effect in noncollinear antiferromagnets Mn_3X ($\text{X} = \text{Rh, Ir, Pt}$). *Phys. Rev. B* **92**, 144426 (2015).

13. Higo, T. *et al.* Large magneto-optical Kerr effect and imaging of magnetic octupole domains in an antiferromagnetic metal. *Nature Photon* **12**, 73–78 (2018).
14. Xia, J., Maeno, Y., Beyersdorf, P. T., Fejer, M. M. & Kapitulnik, A. High resolution polar Kerr effect measurements of Sr₂RuO₄: Evidence for broken time-reversal symmetry in the superconducting state. *Physical Review Letters* **97**, 167002 (2006).
15. Schemm, E. R., Gannon, W. J., Wishne, C. M., Halperin, W. P. & Kapitulnik, A. Observation of broken time-reversal symmetry in the heavy-fermion superconductor UPt₃. *Science* **345**, 190–193 (2014).
16. Gong, X. *et al.* Time-reversal symmetry-breaking superconductivity in epitaxial bismuth/nickel bilayers. *Sci. Adv.* **3**, e1602579 (2017).
17. Choi, Y.-G. *et al.* Observation of the orbital Hall effect in a light metal Ti. *Nature* **619**, 52–56 (2023).
18. Mazin, I. & The PRX Editors. Editorial: Altermagnetism-A New Punch Line of Fundamental Magnetism. *Phys. Rev. X* **12**, 040002 (2022).
19. Amin, O. J. *et al.* Nanoscale imaging and control of altermagnetism in MnTe. *Nature* **636**, 348–353 (2024).
20. Jungwirth, T., Marti, X., Wadley, P. & Wunderlich, J. Antiferromagnetic spintronics. *Nature Nanotech* **11**, 231–241 (2016).
21. Baltz, V. *et al.* Antiferromagnetic spintronics. *Rev. Mod. Phys.* **90**, (2018).
22. Šmejkal, L., Mokrousov, Y., Yan, B. & MacDonald, A. H. Topological antiferromagnetic spintronics. *Nature Phys* **14**, 242–251 (2018).
23. He, Q. L., Hughes, T. L., Armitage, N. P., Tokura, Y. & Wang, K. L. Topological spintronics and magnetoelectronics. *Nat. Mater.* **21**, 15–23 (2022).
24. Feng, W. *et al.* Topological magneto-optical effects and their quantization in noncoplanar antiferromagnets. *Nat Commun* **11**, 118 (2020).

25. Zhang, S.-S., Ishizuka, H., Zhang, H., Halász, G. B. & Batista, C. D. Real-space Berry curvature of itinerant electron systems with spin-orbit interaction. *Phys. Rev. B* **101**, (2020).
26. Zhou, X., Feng, W., Yang, X., Guo, G.-Y. & Yao, Y. Crystal chirality magneto-optical effects in collinear antiferromagnets. *Phys. Rev. B* **104**, 024401 (2021).
27. Vanderbilt, D. *Berry Phases in Electronic Structure Theory*. (Cambridge University Press, Cambridge, 2018).
28. Park, P. *et al.* Field-tunable toroidal moment and anomalous Hall effect in noncollinear antiferromagnetic Weyl semimetal Co_{1/3}TaS₂. *npj Quantum Mater.* **7**, 42 (2022).
29. Park, P. *et al.* Tetrahedral triple-Q magnetic ordering and large spontaneous Hall conductivity in the metallic triangular antiferromagnet Co_{1/3}TaS₂. *Nat Commun* **14**, 8346 (2023).
30. Takagi, H. *et al.* Spontaneous topological Hall effect induced by non-coplanar antiferromagnetic order in intercalated van der Waals materials. *Nat. Phys.* **19**, 961–968 (2023).
31. Parkin, S. S. P. & Friend, R. H. 3d transition-metal intercalates of the niobium and tantalum dichalcogenides. I. Magnetic properties. *Philosophical Magazine B* **41**, 65–93 (1980).
32. Miyadai, T. *et al.* Magnetic properties of Cr_{1/3}NbS₂. *J. Phys. Soc. Jpn.* **52**, 1394–1401 (1983).
33. Parkin, S. S. P., Marseglia, E. A. & Brown, P. J. Magnetic structure of Co_{1/3}NbS₂ and Co_{1/3}TaS₂. *J. Phys. C: Solid State Phys.* **16**, 2765–2778 (1983).
34. Morosan, E. *et al.* Sharp switching of the magnetization in Fe_{1/4}TaS₂. *Phys. Rev. B* **75**, (2007).
35. Xie, L. S., Husremović, S., Gonzalez, O., Craig, I. M. & Bediako, D. K. Structure and Magnetism of Iron- and Chromium-Intercalated Niobium and Tantalum Disulfides. *J. Am. Chem. Soc.* **144**, 9525–9542 (2022).
36. Wu, S. *et al.* Highly Tunable Magnetic Phases in Transition-Metal Dichalcogenide Fe_{1/3+δ}NbS₂. *Phys. Rev. X* **12**, (2022).

37. Ghimire, N. J. *et al.* Large anomalous Hall effect in the chiral-lattice antiferromagnet CoNb₃S₆. *Nat Commun* **9**, 3280 (2018).
38. Khanh, N. D. *et al.* Gapped nodal planes and large topological Nernst effect in the chiral lattice antiferromagnet CoNb₃S₆. *Nat Commun* **16**, 2654 (2025).
39. Cheong, S.-W. & Huang, F.-T. Altermagnetism with non-collinear spins. *npj Quantum Mater.* **9**, 1–6 (2024).
40. Xia, J. *et al.* Polar Kerr-effect measurements of the high-temperature YBa₂Cu₃O_{6+x} superconductor: Evidence for broken symmetry near the pseudogap temperature. *Physical Review Letters* **100**, (2008).
41. Thomas, S. *et al.* Localized Control of Curie Temperature in Perovskite Oxide Film by Capping-Layer-Induced Octahedral Distortion. *Phys. Rev. Lett.* **119**, 177203 (2017).
42. Feng, Z. *et al.* Nonvolatile Nematic Order Manipulated by Strain and Magnetic Field in a Layered Antiferromagnet. Preprint at <https://doi.org/10.48550/arXiv.2507.05486> (2025).
43. Xia, J., Beyersdorf, P. T., Fejer, M. M. & Kapitulnik, A. Modified Sagnac interferometer for high-sensitivity magneto-optic measurements at cryogenic temperatures. *Appl Phys Lett* **89**, 062508 (2006).
44. Onsager, L. Reciprocal Relations in Irreversible Processes. I. *Physical Review* **37**, 405–426 (1931).
45. Nakatsuji, S., Kiyohara, N. & Higo, T. Large anomalous Hall effect in a non-collinear antiferromagnet at room temperature. *Nature* **527**, 212–215 (2015).
46. Kim, M., Freeman, A. J. & Wu, R. Surface effects and structural dependence of magneto-optical spectra: Ultrathin Co films and CoPt alloys and multilayers. *Phys. Rev. B* **59**, 9432–9436 (1999).
47. Park, P. *et al.* Composition dependence of bulk properties in the Co-intercalated transition metal dichalcogenide Co_{1/3}TaS₂. *Phys. Rev. B* **109**, L060403 (2024).

48. Verma, N., Addison, Z. & Randeria, M. Unified theory of the anomalous and topological Hall effects with phase-space Berry curvatures. *Sci. Adv.* **8**, (2022).
49. Erskine, J. L. & Stern, E. A. Magneto-optic Kerr Effect in Ni, Co, and Fe. *Phys. Rev. Lett.* **30**, 1329–1332 (1973).
50. Kato, Y. D., Okamura, Y., Hirschberger, M., Tokura, Y. & Takahashi, Y. Topological magneto-optical effect from skyrmion lattice. *Nat Commun* **14**, 5416 (2023).

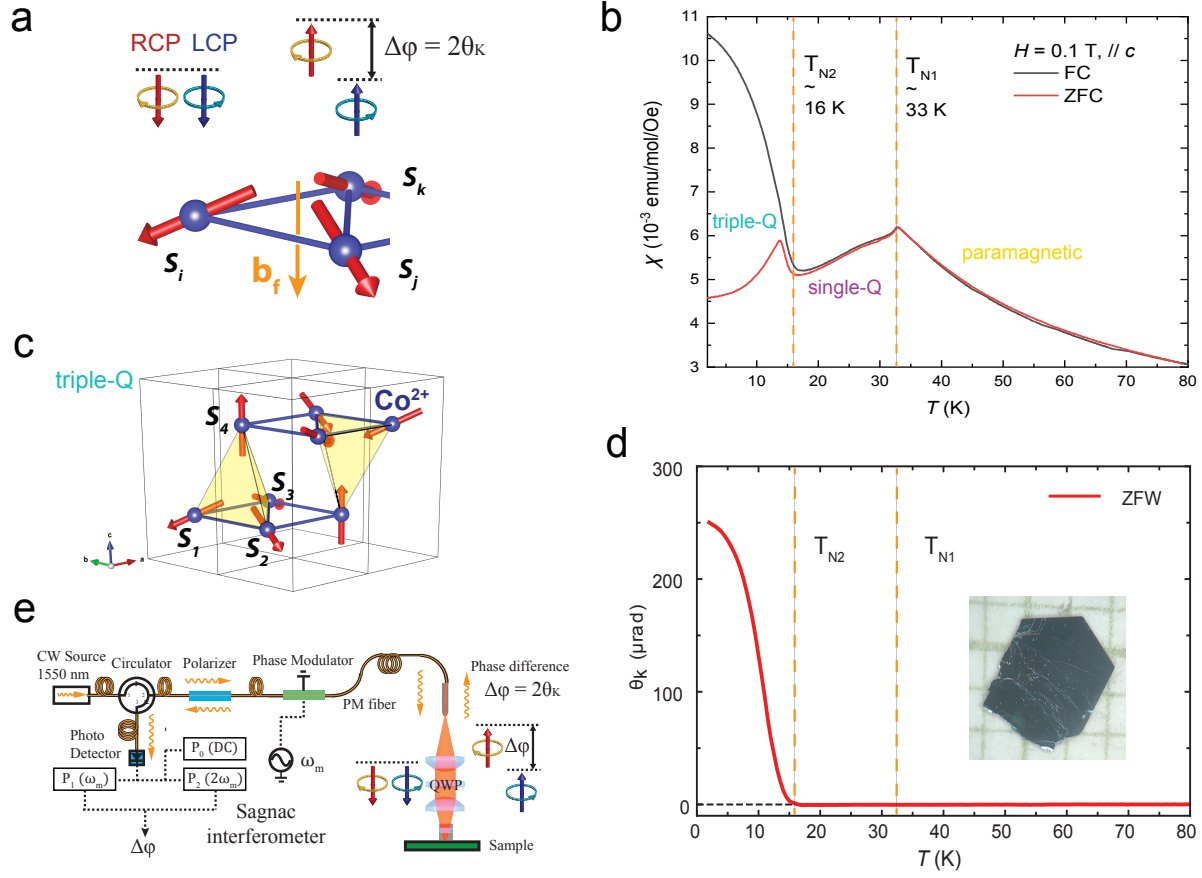


Figure 1. Large MOKE in non-coplanar triple-Q state of $\text{Co}_{1/3}\text{Ta}_1\text{S}_2$. (a) MOKE due to a new topological light-matter interactions in a minimal chiral magnet comprising three neighboring noncoplanar spins. b_f is the fictitious magnetic field generated by the scalar spin chirality $\chi_{ijk} = \mathbf{S}_i \cdot (\mathbf{S}_j \times \mathbf{S}_k)$. MOKE θ_K is a result of the phase difference $\Delta\varphi = 2\theta_K$ between reflected left and right-circularly polarized (LCP and RCP) light. (b) Magnetization M_z measured after field cool (FC) and zero-field cool (ZFC). (c) The tetrahedral triple-Q state of $\text{Co}_{1/3}\text{Ta}_1\text{S}_2$. (d) MOKE θ_K measured during ZFW after 0.3 T FC. Inset is a sample photo on 1 mm grid paper. (e) Schematics of a zero-area-loop Sagnac interferometer microscope for polar MOKE measurements.

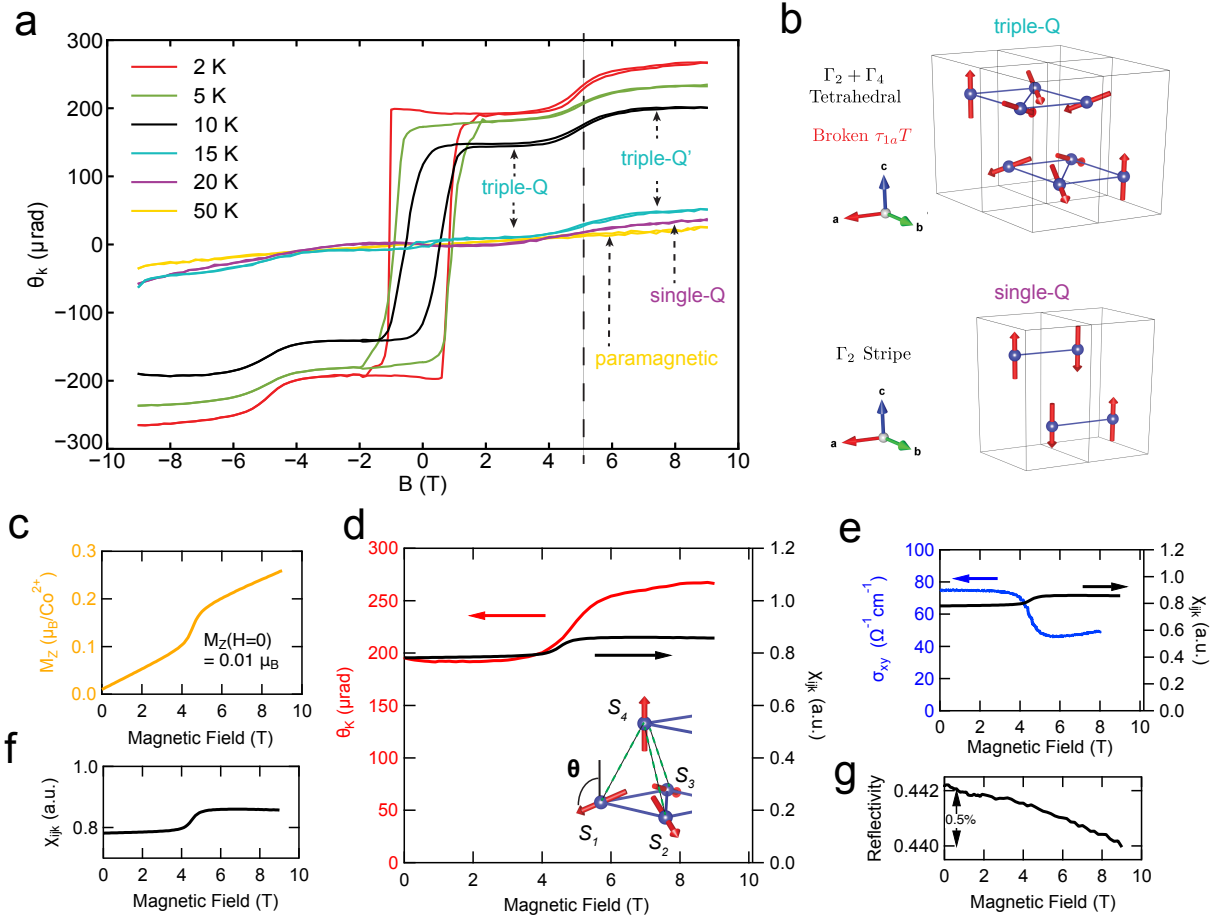


Figure 2. MOKE hysteresis. (a) MOKE hysteresis taken at spot 1 at various temperatures. (b) sketches of triple-Q and single-Q phases. (c) Magnetization M_z at 2 K. (d) MOKE at 2 K plotted with the estimated spin chirality χ_{ijk} . (e) Hall conductivity σ_{xy} at 2 K plotted with χ_{ijk} . (f) Spin chirality χ_{ijk} estimated from magnetization. (g) Reflectivity at 2 K.

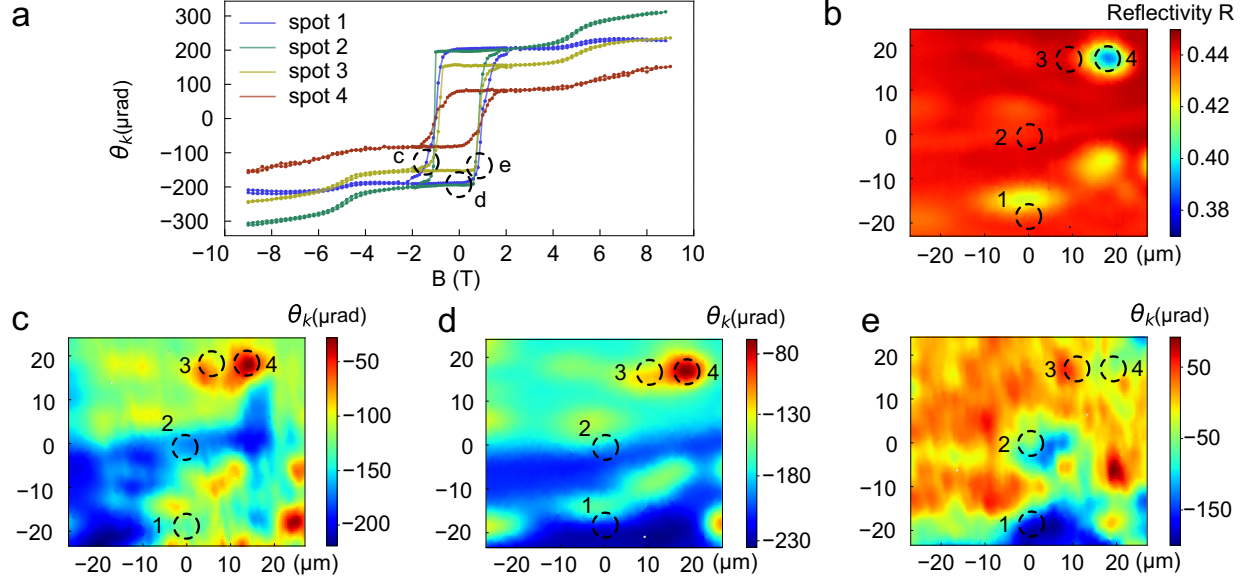


Figure 3. Scalar spin chirality domains imaged at 2K. (a) MOKE hysteresis measured at spots 1-4 at $T = 2$ K. (b) Optical reflectivity image at $T = 2$ K. (c), (d), (e) MOKE θ_K images taken at $B = -1$ T, 0 T, and 0.8 T respectively during the hysteresis loop at $T = 2$ K, showing the formation of scalar spin chirality χ_{ijk} domains.

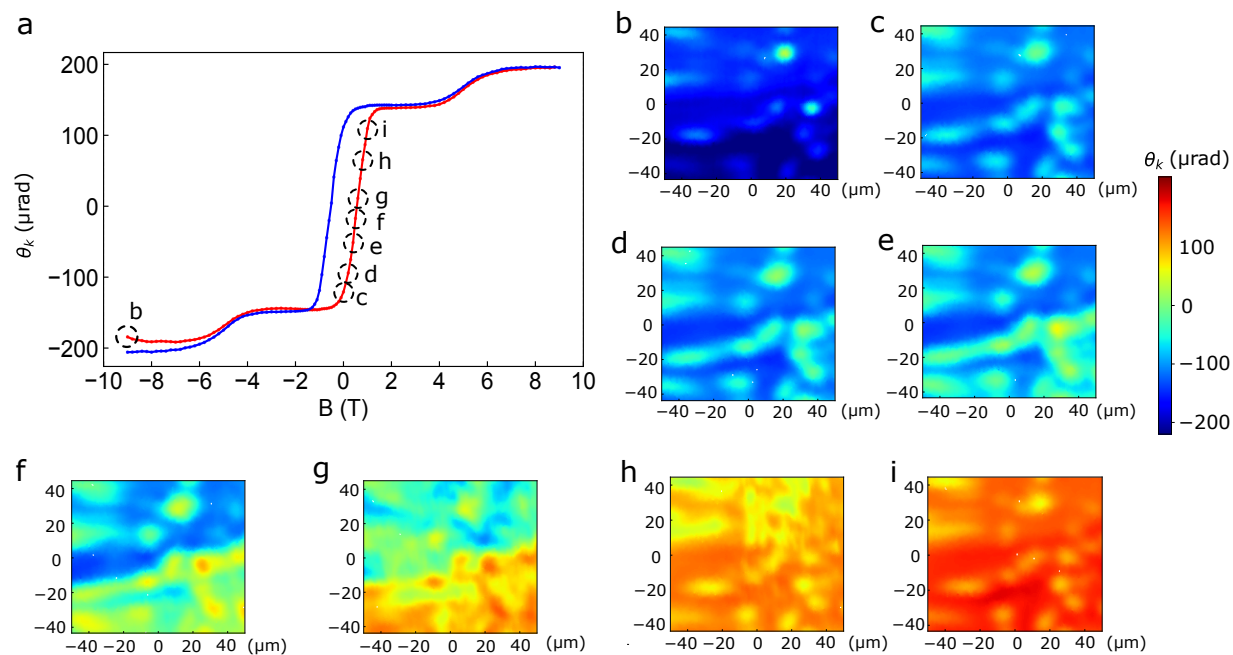
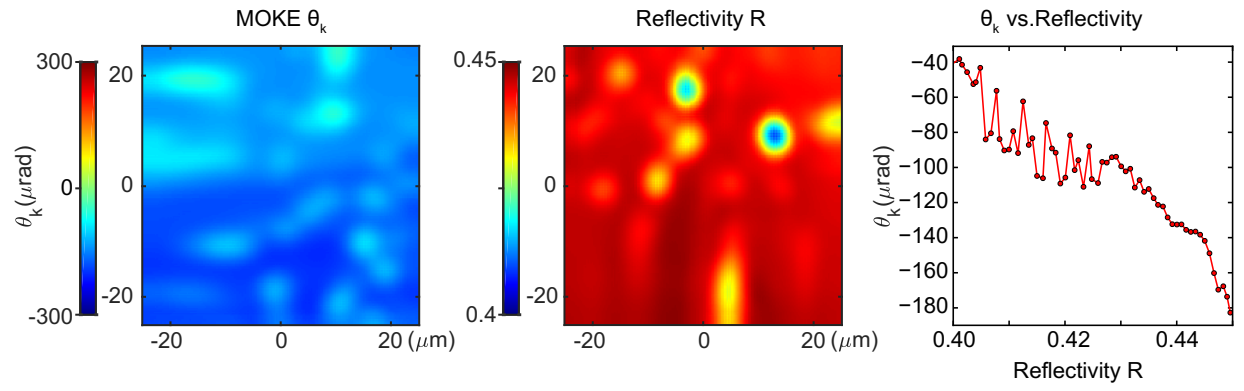
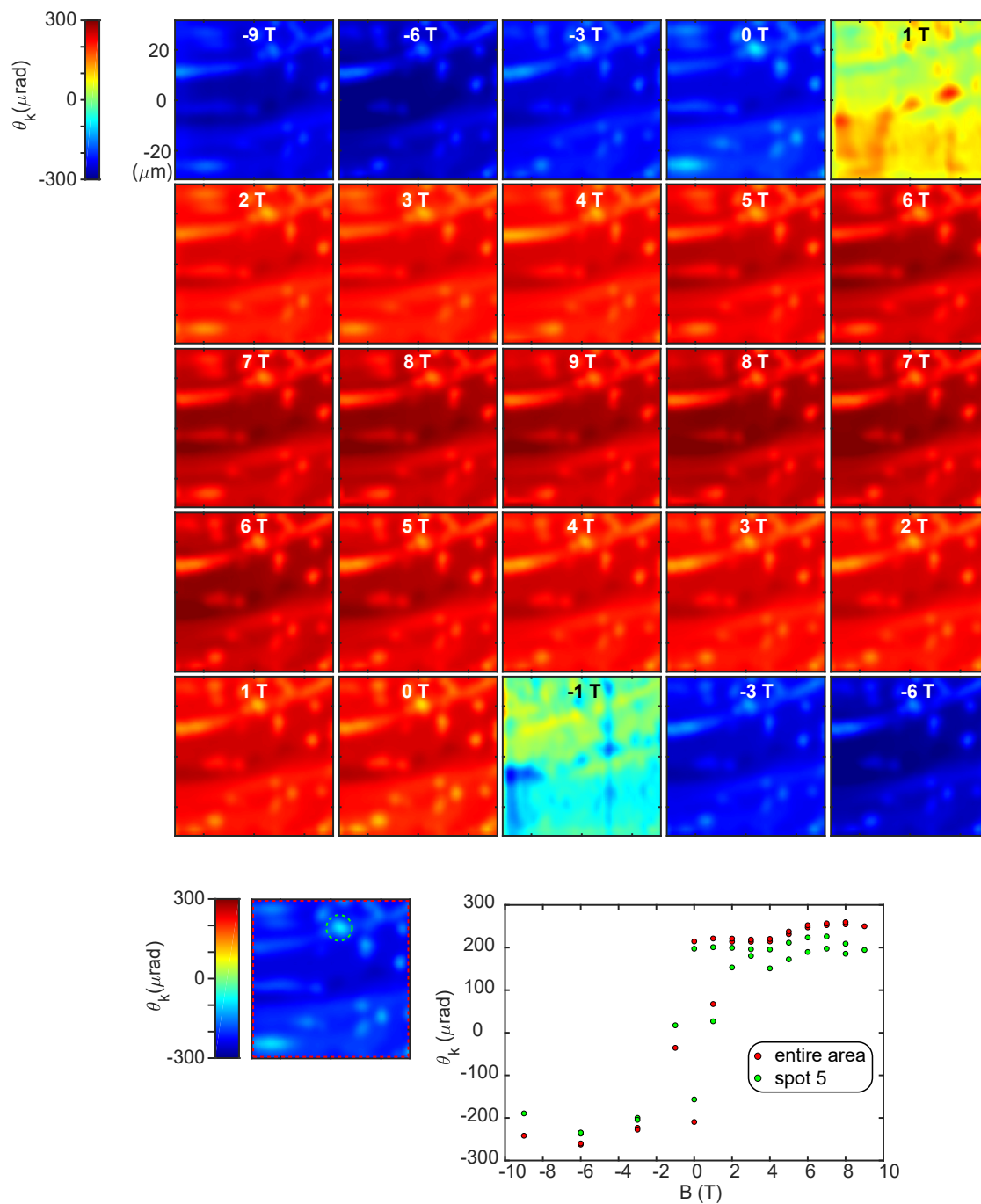


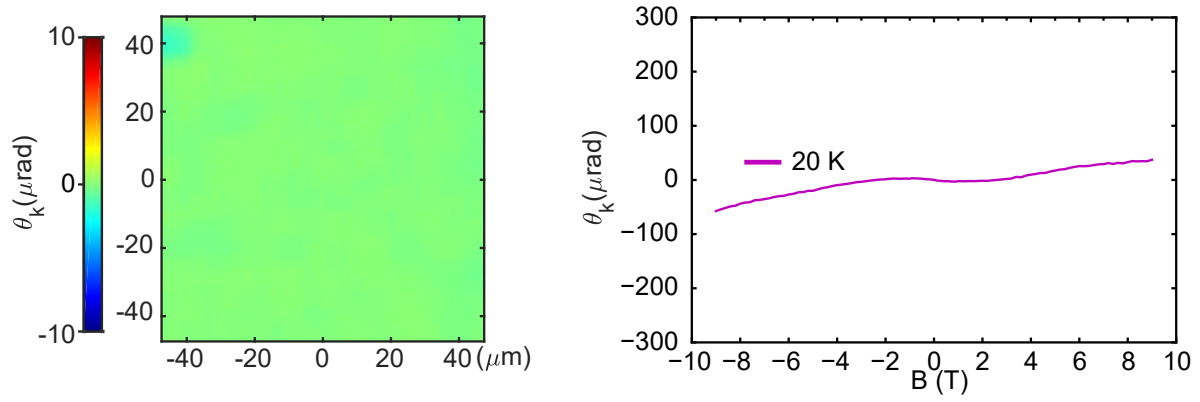
Figure 4. Chirality domain reversal imaged at 10 K. (a) MOKE hysteresis measured at a single spot of the imaged region at $T = 2$ K. **(b) - (i)** MOKE images of chirality domain reversal via domain wall motion at $T = 10$ K.



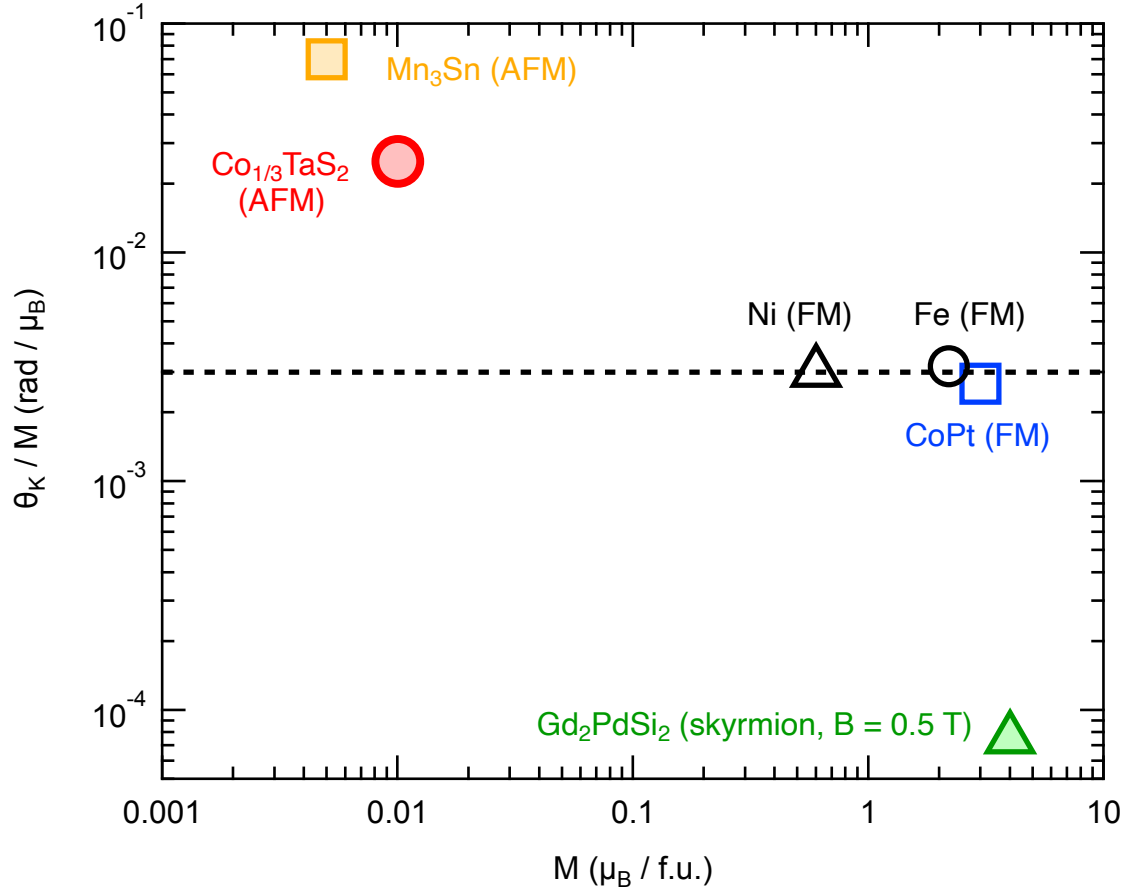
Extended Data Figure 1. Imaging the correlation between co composition and magnetism at 10 K. Spontaneous MOKE image (left), reflectivity image (middle), and their empirical correlation (right).



Extended Data Figure 2. Chirality domain switching in another region at 10K. Top: MOKE images taken during hysteresis at $B = 1\text{T}$ interval. Bottom: extracted hysteresis loop from the whole area average and from the circled spot 5.



Extended Data Figure 3. Zero-field MOKE imaging and hysteresis at 20 K in the single-Q phase. No spontaneous θ_K is present in either MOKE image or single-point hysteresis.



Extended Data Figure 4. MOKE over Magnetization ratio (θ_K/M) of representative ferromagnets (FM), antiferromagnets (AFM), and skyrmion lattice. Ferromagnets (Ni⁴⁹, Fe⁴⁹, and CoPt⁴⁶) have spontaneous θ_K roughly proportional to the magnetization, $\sim 0.03 \text{ rad}/\mu_B$. Noncoplanar antiferromagnet $\text{Co}_{1/3}\text{TaS}_2$ and coplanar antiferromagnet Mn_3Sn ¹³ have negligible net moments and are significantly above this ratio. Skyrmion lattice Gd_2PdSi_2 ⁵⁰ is established only within a narrow magnetic field range near $B = 0.5 \text{ T}$ and is way below this ratio.